

RESEARCH ARTICLE

10.1002/2014JB011261

Key Points:

- Reconciling various observations of the TO earthquake into a single-source model
- Relating slip distribution to various independent observations
- Proposing a rupture scenario

Supporting Information:

- Readme
- Kinematic solution in CMT format
- Figures S1–S10 and Table S1

Correspondence to:

Q. Bletery,
bletery@geoazur.unice.fr

Citation:

Bletery, Q., A. Sladen, B. Delouis, M. Vallée, J.-M. Nocquet, L. Rolland, and J. Jiang (2014), A detailed source model for the M_w 9.0 Tohoku-Oki earthquake reconciling geodesy, seismology, and tsunami records, *J. Geophys. Res. Solid Earth*, 119, doi:10.1002/2014JB011261.

Received 9 MAY 2014

Accepted 31 AUG 2014

Accepted article online 6 SEP 2014

A detailed source model for the M_w 9.0 Tohoku-Oki earthquake reconciling geodesy, seismology, and tsunami records

Quentin Bletery¹, Anthony Sladen¹, Bertrand Delouis¹, Martin Vallée², Jean-Mathieu Nocquet¹, Lucie Rolland^{1,3}, and Junle Jiang⁴

¹Observatoire de la Côte d'Azur, Géoazur UMR 7329, Université de Nice Sophia Antipolis, CNRS, IRD, Nice, France,

²Institut de Physique du Globe de Paris, Sorbonne Paris Cité, Université Paris Diderot, UMR 7154 CNRS, Paris, France,

³Now at Los Alamos National Laboratory, Los Alamos, New Mexico, USA, ⁴Seismological Laboratory, Division of Geological and Planetary Sciences, California Institute of Technology, Pasadena, California, USA

Abstract The 11 March 2011 M_w 9.0 Tohoku-Oki earthquake was recorded by an exceptionally large amount of diverse data offering a unique opportunity to investigate the details of this major megathrust rupture. Many studies have taken advantage of the very dense Japanese onland strong motion, broadband, and continuous GPS networks in this sense. But resolution tests and the variability in the proposed solutions have highlighted the difficulty to uniquely resolve the slip distribution from these networks, relatively distant from the source region, and with limited azimuthal coverage. In this context, we present a finite fault slip joint inversion including an extended amount of complementary data (teleseismic, strong motion, high-rate GPS, static GPS, seafloor geodesy, and tsunami records) in an attempt to reconcile them into a single better resolved model. The inversion reveals a patchy slip distribution with large slip (up to 64 m) mostly located updip of the hypocenter and near the trench. We observe that most slip is imaged in a region where almost no earthquake was recorded before the main shock and around which intense interplate seismicity is observed afterward. At a smaller scale, the largest slip pattern is imaged just updip of an important normal fault coseismically activated. This normal fault has been shown to be the mark of very low dynamic friction allowing extremely large slip to propagate up to the free surface. The spatial relationship between this normal fault and our slip distribution strengthens its key role in the rupture process of the Tohoku-Oki earthquake.

1. Introduction

The 11 March 2011 M_w 9.0 Tohoku-Oki earthquake (TO) is, given its magnitude and the available instrumentation, an unprecedented opportunity to investigate the details of a seismic rupture in a subduction zone. It has been the object of numerous studies based on different subsets of the available data, leading to various coseismic slip models.

If we try to extract the main features of those models [Iinuma *et al.*, 2011; Koketsu *et al.*, 2011; Miyazaki *et al.*, 2011; Ozawa *et al.*, 2011; Yokota *et al.*, 2011], we find that static-only solutions, inferred from the exceptionally dense onland GPS network, tend to place the maximum slip either downdip of the hypocenter or just beneath it. But the GPS station's concentration westward from the rupture likely causes a bias in the solutions. The addition of data closer to the rupture, such as seafloor motion obtained from shifts in locations of GPS-Acoustic or ocean bottom seismometer stations [Sato *et al.*, 2011; Kido *et al.*, 2011], or from offsets in reflection profiles [Fujiwara *et al.*, 2011], tends to force most of the slip distribution to occur updip of the hypocenter [Ito *et al.*, 2011; Iinuma *et al.*, 2012; Perfettini and Avouac, 2014]. The coverage limitation have led studies to also incorporate tsunami records into slip inversions. With the addition of tsunami data, these joint static solutions obtained from optimization also tend to place most of the slip between the hypocenter and the trench [Romano *et al.*, 2012; Hooper *et al.*, 2013; Yokota *et al.*, 2011; Minson *et al.*, 2014] (with the exception of Simons *et al.*'s [2011] model probably due to overfitting the GPS data [Minson *et al.*, 2014]). This tendency of shallow large slip is also found in tsunami-only inversions [Koketsu *et al.*, 2011; Yokota *et al.*, 2011; Maeda *et al.*, 2011; Saito *et al.*, 2011; Melgar and Bock, 2013]. This suggests that, thanks to their sensitivity to the whole surface deformation field, tsunami observations provide better constraints on the shallow part of the fault than other techniques and predict [Lay *et al.*, 2011a; Yokota *et al.*, 2011; Romano *et al.*, 2012; Hooper *et al.*, 2013]—or are explained by [Fujii *et al.*, 2011; Yamazaki *et al.*, 2011a, 2013]—large slip there.

Kinematic inversions, that are inferred from seismic waves (teleseismic P or S wave and near-field strong motion accelerograms) or high-rate continuous GPS (HRGPS) time series, have also shown a consistent large-scale large-slip region updip of the hypocenter close to the trench [Hayes, 2011; Ide et al., 2011; Lay et al., 2011b; Shao et al., 2011; Yoshida et al., 2011, 2012; Wei et al., 2012; Yue and Lay, 2013]. This consistent trend in the models arises despite some inherent limitations in the data used: teleseismic data provide a coarse resolution on the slip distribution—especially when the data do not exhibit strong directivity on which is based the spatial resolution—and both strong motion accelerograms and HRGPS observations have very limited azimuthal coverage causing the resolution to drop dramatically toward the trench [Wei et al., 2012; Yue and Lay, 2013]. Additionally, tsunami observations, usually treated as static data, have recently been suggested to contain kinematic information in the case of TO [Satake et al., 2013]. Indeed, the usual assumption of a seismic rupture infinitely faster than the tsunami wave propagation is challenged in the trench area by a very large column of water (≈ 8 km)—resulting in a faster wave propagation (tsunami velocity is proportional to the square root of the water depth)—associated with a suspected slower seismic rupture in this same superficial region. Satake et al. [2013] showed that treating tsunami observations as kinematic data allows longer rupture scenarios with possible large shallow slip farther north.

Joint inversions including part or most of the static and kinematic data [Koketsu et al., 2011; Yokota et al., 2011; Ammon et al., 2011; Lee et al., 2011; Lay et al., 2011b; Yue and Lay, 2013; Wei et al., 2012; Minson et al., 2014] are expected to converge on a slip model because more data should reduce the null space. However, these inversions are still not able to converge on a coherent slip pattern. We propose three explanations for this discrepancy: (1) the nonuniqueness of the solution considering partial data sets with limited azimuthal coverage; (2) the different modeling approaches (fault and time parametrization, regularization in inversion procedure, etc.) varying from one study to another; and (3) the covariance between inverted data and weighting approaches [Duputel et al., 2014]. In this study, we include all suitable data (static GPS, seafloor geodesy, teleseismic, strong motion, HRGPS, and tsunami records) into a single joint inversion. Our main purpose here is to find a slip model explaining all the observations. If such a model exists, the quantity of explained data should greatly reduce the nonuniqueness of the solution and the inversion should reveal robust slip patterns.

2. Data

In our inversion, we include static GPS data, seafloor geodesy, HRGPS, accelerograms, teleseismic, and tsunami records. We choose to not include interferometric synthetic aperture radar data because it contains postseismic signal and its information content is redundant with the dense GPS GEONET Japanese network's measurements which is assumed to provide data with less ambiguity [Feng and Jónsson, 2012].

2.1. Teleseismic Broadband Data

We use 20 broadband seismograms of the main shock recorded at teleseismic distances (station locations are shown in Figure S4 in the supporting information), obtained from the Incorporated Research Institutions for Seismology (IRIS) data center. Inverted records are displacement waveforms windowed around the P (vertical) and SH wave train (only for five seismograms). Data processing includes deconvolution from the instrument response, integration to obtain displacement, equalization to a common magnification and epicentral distance, and band-pass filtering from 0.01 Hz to 0.8 Hz (P waves) or to 0.4 Hz (SH waves).

2.2. Accelerograms

We use 42 time series (14 stations times three components; station locations are shown in Figure S5), retrieved from the strong motion Japanese network K-NET National Research Institute for Earth Science and Disaster Prevention (NIED) data center (<http://www.kyoshin.bosai.go.jp>). Acceleration records were integrated to displacement and band pass-filtered between 0.01 and 0.08 Hz. The relatively low high-cut frequency is adapted to the large size of the event while the low-cut frequency is necessary because we invert displacements from acceleration data and the double integration introduces noise at very low frequency. Exceptionally, the low-cut frequency was raised to 0.02 or 0.03 Hz instead of 0.01 Hz if some residual noise was detected.

2.3. High-Rate GPS Data

We process a time window of 2 h of 1 Hz data from the GEONET network of the Geospatial Information Authority (GSI) of Japan. We selected a subset of 28 sites located from latitude 36 to latitude 44, providing the best possible azimuthal coverage of the rupture area (see station locations in Figures S6 and S7).

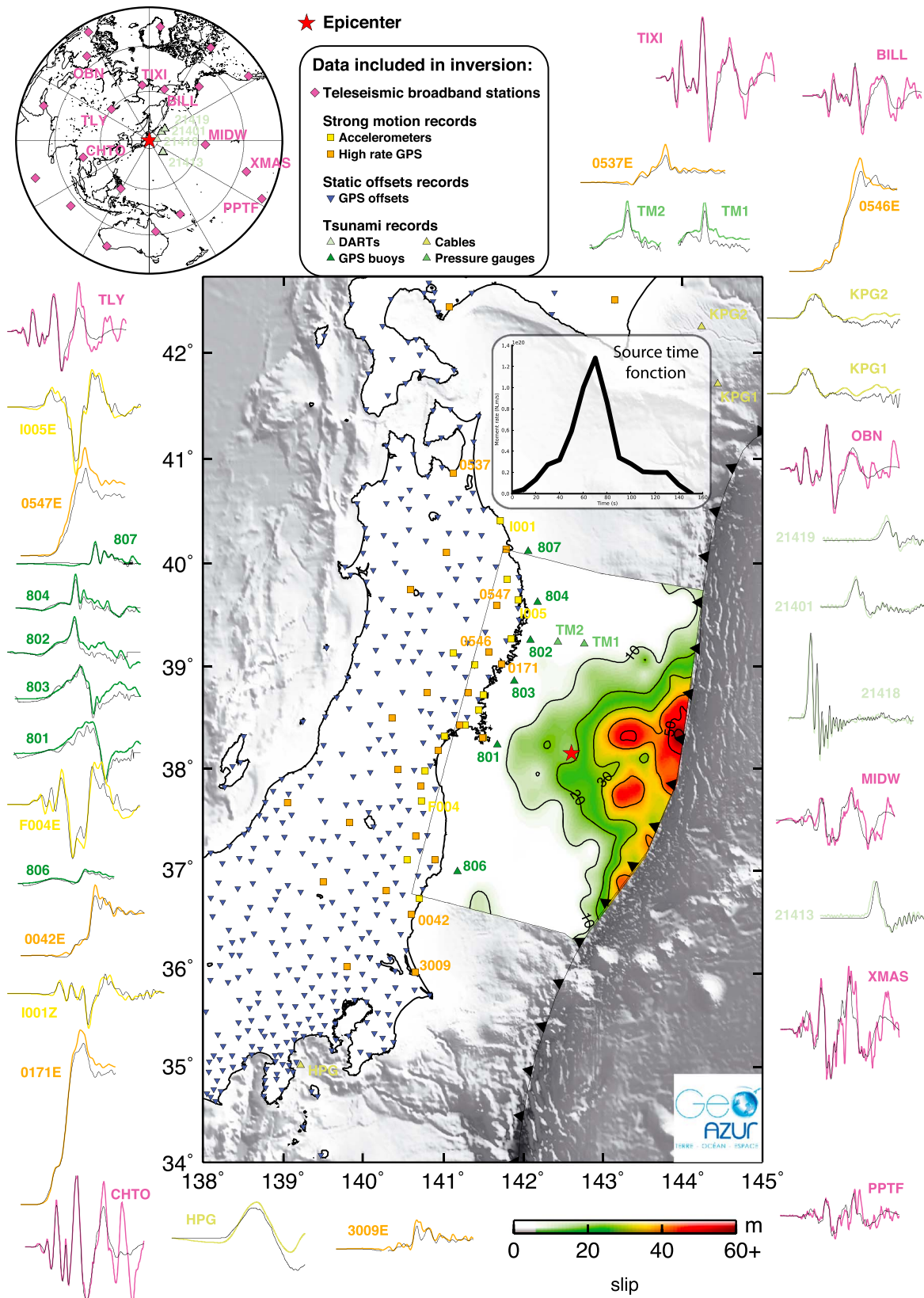


Figure 1. Preferred slip model obtained by inversion of the undermentioned data sets: teleseismic, accelerograms, HRGPS, static GPS, and tsunami records. The associated source time function is shown in the top right corner. Station locations are represented by data sets (see legend for details). Colored curves show data fits at sampled stations (colored is observed, black is predicted). Colors correspond to data types. See Figures 3, 4, and S4–S7 for complete data fit plots.

We used three independent software packages for GPS kinematics analysis (GAMIT/Track, Gipsy, and GINS) and check consistency among results. One-sample-per-second high-rate GPS time series were then filtered using a low-pass filter below 0.08 Hz (conserving the static component) for horizontal components and a band-pass filter between 0.01 Hz and 0.08 Hz (as for accelerograms) for the vertical component because of its higher inaccuracy.

2.4. Static GPS Data

We use a total of 1221 GPS displacement offsets (407 stations times three components; station locations are shown in Figure 1), computed by the Advanced Rapid Imaging and Analysis (ARIA) team at Jet Propulsion Laboratory/California Institute of Technology (JPL/Caltech) (ftp://sideshow.jpl.nasa.gov/pub/usrs/ARIA_version0.3) using the original 30 s GEONET receiver-independent exchange data provided by the Geospatial Information Authority (GSI) of Japan. We used displacements between a solution at 5:40 and 5:55 UTC, based on 5 min solutions. Estimates of uncertainties are provided in the ARIA solution (see ftp file for details) but are about 16 cm on average for each component.

2.5. Seafloor Geodesy

Seafloor geodesy is very rarely available to study underwater earthquakes and is a great complement to the static GPS to constrain distant offshore slip. Seven seafloor GPS acoustic stations recorded the TO event: KAMS, KAMN, MYGI, MYGW, FUKU [Sato *et al.*, 2011], GJT3, and GJT4 [Kido *et al.*, 2011]. Their measurements provide information very close to the source with a good azimuthal coverage (station locations are shown in Figure S3), but they contain 23, 25, 17, 16, 19, 31, and 31 days of postseismic signal, respectively. Moreover, these measurements also contain pre-Tohoku signal and especially a series of foreshocks—with magnitudes up to $M_w 7.4$ —localized close to the stations [Nettles *et al.*, 2011]. As we are only interested in the coseismic phase, we must assume large uncertainties on these data. And given the location of the measurement points, these uncertainties introduce biases with large weight in the inversion. For this reason, our preferred model does not include the seafloor geodesy measurements. When including these data in the inversion, the slip distribution is similar (Figure S3), except in the region where their stations are located, pleading for important postseismic deformation in this particular region.

2.6. Tsunami Records

We use 15 time series of the tsunami wave height at different points of measurement from four DART (Deep-ocean Assessment and Reporting of Tsunamis) buoys (21418, 21401, 21413, and 21419), six GPS buoys (GPS801, GPS802, GPS803, GPS804, GPS806, and GPS807), two pressure gauges (TM1 and TM2), and three cables (KPG1, KPG2, and HPG). DART records are provided by the NOAA National Geophysical Data Center (http://ngdc.noaa.gov/hazard/dart/2011honshu_dart.html) and have a sampling rate of 1 min. GPS buoys are given by the Nationwide Ocean Wave information network for Ports and Harbours (NOWPHAS) system (http://nowphas.mlit.go.jp/info_eng.html) and have a sampling rate of 5 s. Pressure gauges records are described by Maeda *et al.* [2011]. Cables data are downloaded from the Independent Administrative Institution, Japan Agency for Marine-Earth Science and Technology (JAMSTEC) cabled observatories website (http://www.jamstec.go.jp/scdc/top_e.html); their sampling rate is very high frequency (1 Hz), but we band-pass filter them between 2 min and 50 min to eliminate the effect of wind waves and tides. Station locations are shown in Figure 1. Their azimuthal coverage is very good. In particular, they provide the only robust information east of the source (DARTs). They also provide valuable information north (cables) and close to the source (pressure gauges and GPS buoys).

3. Forward Modeling

3.1. Fault Discretization

The first stage of the problem is the discretization of the considered megathrust fault surface. We subdivide the slab interface into 187 subfaults of variable dimensions, strike, and dip angles (see Figure S1 and Table S1) built to follow the 3-D geometry of the SLAB1.0 model [Hayes *et al.*, 2012]. Because of the shorter wavelength of the deformation pattern near the surface and especially since tsunami data are directly affected by these details, we refine our grid in the shallowest 10 km and build our geometry so that the shallowest subfaults match the free surface at the trench. This level of refinement is indeed critical to properly model both the sea bottom deformation and the tsunami excitation (Q. Bletery *et al.*, Quantification of tsunami bathymetry effect on finite fault slip inversion, submitted to *Pure and Applied Geophysics*, 2014). We considered adding subfaults to model the coseismic normal faulting observed in the hanging wall by

Tsuji et al. [2013]. But after calculation of the response of the static data sets to the 1.1 m of coseismic slip observed by the authors, we found that the effect was significantly below the data resolution.

For each subfault, the theoretical response (Green's function) of every data is calculated for a 1 m displacement both along the dip and strike directions. The modeling of the different data sets relies on different physical processes and is described below by data type.

3.2. Modeling of Seismic Data

To model the seismic waveforms, the continuous rupture is approximated by a summation of point sources, one at the center of each subfault. Synthetic seismograms at local to regional distances (HRGPS and strong motion data) are computed using the discrete wave number method of *Bouchon* [1981] designed for 1-D stratified velocity models. Synthetic seismograms at teleseismic stations are generated using ray theory approximation [*Nabelek*, 1984] considering the 1-D CRUST2.0 global crustal velocity model from *Laske*, *Masters*, and *Reif* (<http://igppweb.ucsd.edu/gabi/rem.html>).

3.3. Modeling of Static Geodetic Data

To model the static coseismic displacement (static GPS and seafloor geodesy), subfaults are represented by dislocation surfaces. The displacements are computed using the formulation of *Savage* [1980] for dislocation embedded in an elastic half-space.

3.4. Modeling of Tsunami Data

Tsunami waveforms are computed in three steps. First, the sea bottom deformation is computed using the dislocation formulation of *Savage* [1980]. Then, we add the contribution of horizontal motion combined with topography (that we will call bathymetry effect (BE)) [*Tanioka and Satake*, 1996] to the obtained vertical displacement field and apply a $1/\cosh(kh)$ filter (where k is the wave number and h the water depth) to the result in order to model the attenuation of the water column [*Kajiura*, 1963]. Finally, we compute the tsunami propagation using the NEOWAVE code [*Yamazaki et al.*, 2009, 2011b] that takes into account dispersive effects. Dispersive effects start to be important for far-field measurements such as those recorded by DART buoys [*Watada*, 2013; *Tsai et al.*, 2013].

4. Inversion Procedure

Using the Green's functions described above, we invert for the coseismic slip distribution in time and space that best explain all the observations previously described. Our kinematic modeling follows the approach described by *Delouis et al.* [2002]. The model hypocenter is—based on a seismic waveform and GPS inversion—imposed at 38.15°N , 142.61°E , and at a depth of 24.5 km (*Chu et al.*'s [2011] location is $(38.19^\circ\text{N}, 142.68^\circ\text{E}, 21\text{ km})$, Japan Meteorological Agency's (JMA) location is $(38.103^\circ\text{N}, 142.861^\circ\text{E}, 24\text{ km})$, and U.S. Geological Survey's (USGS) location is $(38.322^\circ\text{N}, 142.369^\circ\text{E}, 32\text{ km})$).

The source of each subfault in the model is represented by a seismic moment rate function (source time function, STF). In our formulation, the seismic moment rate function is represented by a series of seven triangular functions, isosceles and mutually overlapping over their half duration (6 s). The number of individual triangles (seven) and their width (12 s) are adapted to the magnitude of the earthquake and the size of the subfaults. They are fixed in the inversion and dimensioned to account for the maximum slip duration and maximum duration of local rupture propagation on a single subfault. On the other hand, the amplitude of each of the individual triangular functions is a free (bounded) parameter in the inversion. Such parameterization, with seven overlapping triangles, allows some flexibility in the shape of local source time functions. In total, nine parameters are to be inverted for each subfault: the rake (slip direction), the rupture onset time, and the seven amplitudes of the individual triangular functions. The total number of inverted parameters is then 9×187 subfaults, hence 1663.

Rupture onset times are bounded according to a minimum and a maximum rupture velocity of 1.1 and 3.1 km/s respectively. The rake angle can vary between 60° and 120° in order to smoothly compensate the large strike variations along the fault. The tsunami data are here treated as kinematic data, as the static approximation can lead to significant bias in the inverted slip distribution [*Satake et al.*, 2013].

A nonlinear inversion of all the data sets described previously is performed using a simulated annealing optimization algorithm. The convergence criterion is based on the simultaneous minimization of the root-mean-square (RMS) data misfit and of the total seismic moment. The RMS misfit error is the average of

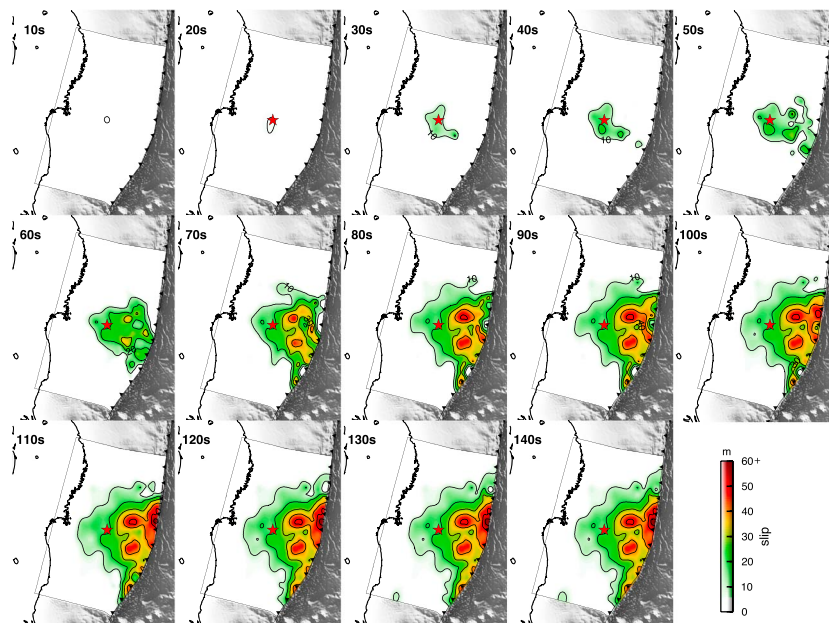


Figure 2. Cumulative rupture snapshots with 10 s time windows. The slip contour in the first time window is 5 m. In all other subfigures slip contours are 10 m intervals.

the normalized RMS errors of the individual data sets (teleseismic, strong motion and HRGPS, static GPS, and tsunami records), equally weighted. Minimization of the total seismic moment is required to reduce spurious slip in the fault model. To convert the obtained moment in displacement, we use the layered Earth model shown in Figure S2 derived from the J-SHIS 3-D tomography data integrated over 1-D for the first 16 km and Takahashi *et al.* [2004] results for the deepest part.

5. Results

5.1. A Patchy Shallow Slip Distribution

The inversion of all these observations—except the seafloor geodesy—reveals a patchy slip distribution with huge shallow slip reaching the free surface. Indeed, as shown in Figure 1, most of the slip is found updip of the hypocenter. The spatial extent of slip appears relatively narrow for a magnitude 9.0 earthquake. However, as we are probably not able to image slip patterns under a few meters of slip, the outer limits of the spatial slip distribution will remain unclear. We truncate our color palette at 6 m which implicitly means that we do not believe in slip patterns below 10% of the maximum slip imaged, but a clear estimation of uncertainties of source inversion is still, as discussed earlier in section 1, an unresolved research problem. Nevertheless, the experience gained from running multiple inversions and synthetic tests (detailed below in section 5.3) leads us to believe that we are able to resolve 60 km long patches with more than 10 m of slip. The distribution is very dissymmetric along dip. The rupture starts from a narrow area around the hypocenter to, at the end, spread over a much wider zone in the shallowest part, reaching the trench with very large amplitudes (60 m). The whole rupture lasts about 150 s with most of the moment released between 50 s and 100 s (see source time function in Figure 1 and nucleation history in Figure 2). Moreover, this slip model predicts the 50 m of horizontal motion measured at the trench by Fujiwara *et al.* [2011], a datum that was not included in the inversion. Outside the shallowest part of the fault, we observe two distinct high-slip patches with a size of the order of 50 to 100 km.

Our model including the seafloor geodesy (Figure S3) is very similar to our preferred model. The only difference between the two source inversions is the exact size and location of the northern-western patch, the region where seafloor geodesy stations are located. This small difference could be explained by residual preshocks (foreshocks) and postseismic signal contained in these measurements and indicates that our preferred slip model is consistent with these independent measurements close to the fault rupture.

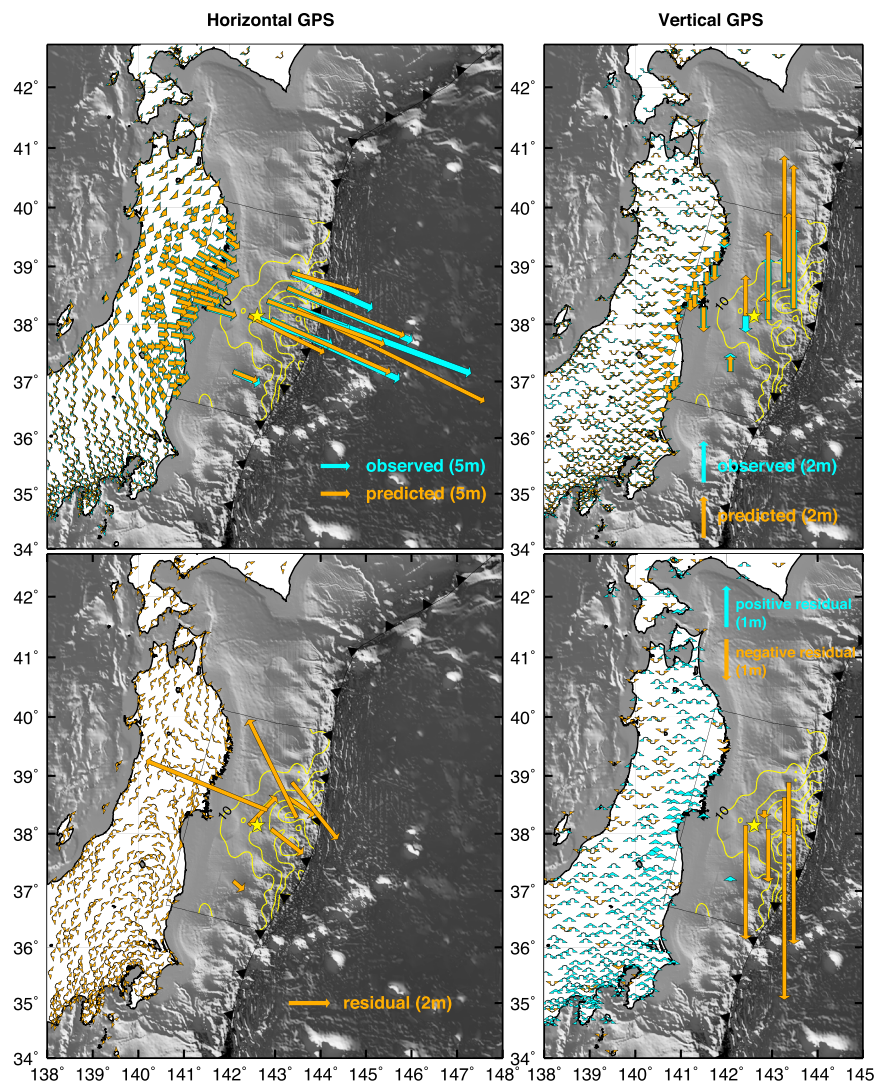


Figure 3. Static GPS and seafloor geodesy data fits. (top) Observed (blue) compared to predicted (orange) by our preferred slip model; left is horizontal and right vertical. (bottom) Residual (observed-predicted). For vertical residual, blue is pointing up, orange pointing down. The seafloor geodetic data were not included in the inversion of our preferred slip model: they are shown for a posteriori comparison. Residuals of the GPS data are below (<15 cm) the data uncertainties (~16 cm), and even though seafloor geodesy measurements were not included in the inversion, their fit is fair.

The seismic moment associated with our preferred slip model is $M_0 = 3.53 \cdot 10^{29}$ dyn cm ($M_0 = 3.59 \cdot 10^{29}$ dyn cm for the other one) corresponding to a magnitude $M_w = 9.0$ (in both cases). These values are consistent with the global centroid moment tensor solution which estimated a moment $M_0 = 5.31 \cdot 10^{29}$ dyn cm and a magnitude $M_w = 9.1$ from mantle waves.

5.2. Data Fit

A subset of different waveform fits is shown in Figure 1—colors corresponding to different data types, with symbols indicating station locations—and illustrates the excellent fit obtained with all the data sets. Figures 3, 4, and S4–S7 show the complete data fits for all data types. Agreement between observations and predicted data is given in Table 1.

The GPS observations are well fitted (Figure 3), and the residuals are lower (< 15 cm) than data uncertainties (~16 cm). Although not included in the inversion, seafloor geodesy measurements are fairly well explained by our model (Figure 3). The vertical residuals show a coherent subsidence pattern over the different stations while the horizontal residuals show a more chaotic pattern (Figure 3, left and right columns).

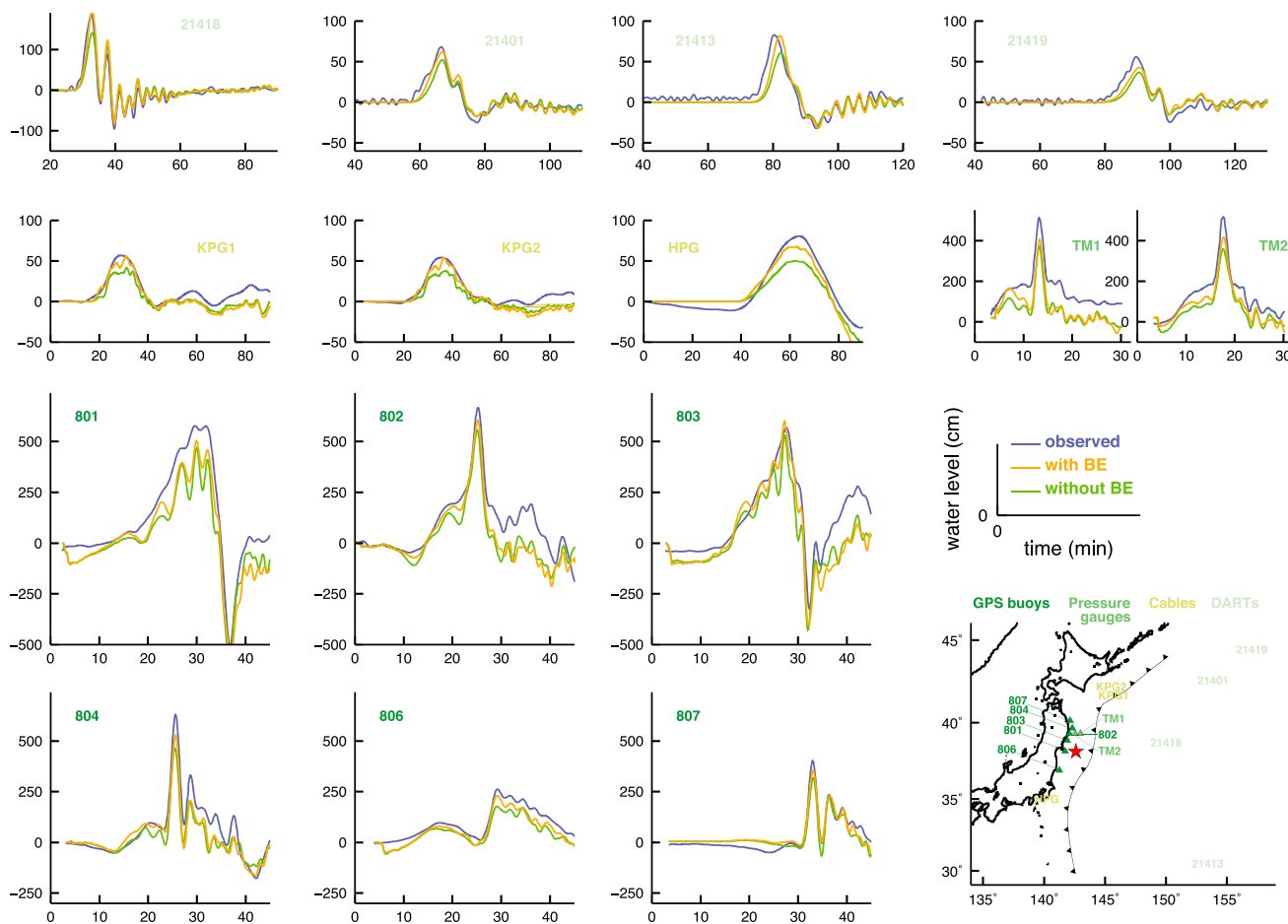


Figure 4. Tsunami data fit. Blue is observed, orange is predicted by inversion taking into account the bathymetry effect (BE), and green is predicted by an inversion not taking into account. We explain better the data with this effect. This attests that tsunami physics accounting for BE improves its consistency with other observations.

These patterns may have different origins. Other studies resulted in similar patterns in the horizontal and vertical residuals [e.g., *Simons et al., 2011*]. As *Simons et al. [2011]*, we favor the hypothesis that these residuals are caused by model errors. Another possible source of error is the heterogeneity of time windows between data sets with the seafloor geodesy measurements including part of the foreshock and postseismic sequences.

In addition to the tsunami data fit (Figure 4) obtained by our preferred model, we show the data fit obtained by a separate inversion (green curves in Figure 4) that uses the exact same data sets and parameterization with the exception that the tsunami Green’s functions do not take into account the BE. In this case, the agreement goes down to 52% (instead of 57%) with no significant change to the final slip model. We explain this change in the fit of the tsunami by a better compatibility with information given by other data sets when we include the BE into tsunami Green’s functions. It is a strong evidence of the improvement in tsunami modeling accuracy when BE is accounted for. We notice that the synthetics show higher frequency

than the data. This could be an artifact of the wave propagation calculation and has been discussed by the authors of the NEOWAVE tsunami simulation code [*Yamazaki et al., 2011a, 2013*]. But two additional effects might come into play: (1) data are acquired at a low sampling rate or are low-pass filtered but might

Table 1. Agreement Between Observed and Predicted Data

Data Type	Agreement $\left(1 - \sum \left \frac{\text{observed} - \text{predicted}}{\text{observed}} \right \right)$
Teleseismic	54%
Accelerograms and HRGPS	90%
Static GPS	94%
Tsunami	57%

intrinsically contain high frequencies and (2) rectangular subfault discretization introduces unphysical borders that could create high frequencies in predicted tsunami time series, especially for subfaults near the free surface.

5.3. Resolution Tests

In order to evaluate the robustness of our inversion, we perform a resolution test (Figure S8). We first consider a patchwork composed of 60 km long square patches (Figure S8, top) and calculate the synthetic data produced by this slip pattern. We then invert them jointly (with the exception of seafloor geodesy data that are not included in order to reproduce the conditions of our preferred model) to see how well we are able to recover the target. The inversion recovers well the input pattern for the entire fault, giving an idea of our resolution assuming perfect data prediction. The checkerboard input pattern is challenging to recover, especially for kinematic data: signals generated by similar patches homogeneously distributed around the hypocenter generate similar waveforms, both in phase and amplitude, making them extremely hard to distinguish from each other.

Nevertheless, this first test was conclusive and indicates that the resolution of our problem might be equal or finer than the 60 km length of the patches. Thus, we performed a second test with smaller slip patches (30 km long instead of 60 km). In this case, the patchwork is not recovered everywhere (Figure S8, bottom): it is mainly recovered in the northern shallow part of the fault. This results might appear at odds with the density of observations along the coast and right above the deeper part of the fault. And because the density of onland stations is homogeneous all along the fault, the increased resolution in the north can only be explained by the higher density of tsunami stations. Because tsunami data are linearly related to the seafloor deformation, they are equivalent to near-field observations when the earthquake rupture is shallow, even if the tsunami wave is measured hundreds of kilometers away. As a consequence, denser onland instrumentation will not improve resolution on the megathrust and deep subfaults will never be as well resolved with surface data.

To investigate these resolution considerations a bit further, we also present, in Figure S9, a series of separated checkerboard tests for the different data sets (the last subfigure is different from Figure S8, because it includes the seafloor geodesy data). Strong motion and HRGPS data inverted jointly give a result similar to the static GPS-only inversion. This is because the horizontal components of HRGPS data contain the static offsets of the static GPS data. Both of these data sets succeed in imaging patches of the considered size close to the coast but fail for the others, highlighting the limitation of onland data to image offshore earthquakes. The difference between the patterns recovered using static GPS only or strong motion and HRGPS data is marginal. Hence, the additional information on the timing of the slip contained in the strong motion and HRGPS data does not seem to greatly reduce the nonuniqueness of the solution, unless the static GPS compensate by the much larger number of data points. Teleseismic data fail to explain the input pattern with the exception of a patch near the coast which is partially imaged. This is due to the too large number of free parameters to invert in view of the data set information content, especially with the considered distributed patchwork, as discussed above. Tsunami data appear to provide by far the best resolution and is the only data set to provide reliable information close to the trench. Seafloor geodesy also provides good resolution over the whole fault because of its central location and proximity to the fault. However, this test is performed without adding any noise in synthetic data. As we suspect seafloor geodesy measurements to contain possible large preseismic/postseismic signal, they are likely to introduce a coherent bias incompatible with ocean bottom deformation predicted by tsunami data. A comparison of Figures S8 and S9 indicates that the resolution of the joint inversion does not suffer from removing the seafloor geodesy. This result supports our choice to exclude the seafloor geodetic data from our main inversion.

5.4. Surface Wave Prediction

We further validate our kinematic source model through a comparison with broadband surface waves recorded at teleseismic stations. To do so, we adopt an empirical Green's function (EGF) approach, using as an EGF the 9 March 2011 M_w 7.4 precursor. Theoretically, the relative source time functions (RSTFs) can be obtained by a direct deconvolution of the EGF signals from the main shock signals [Hartzell, 1978]. However, the inherent instability of the deconvolution operator may contaminate the results. To retrieve more reliable RSTFs, we apply the stabilized deconvolution technique of Vallée [2004], in which four physical constraints on the RSTFs (causality, positivity, limited duration, and equal area) are included in the deconvolution process. Figure S10 shows the Love and Rayleigh waves RSTFs (grey filled curves), obtained from broadband

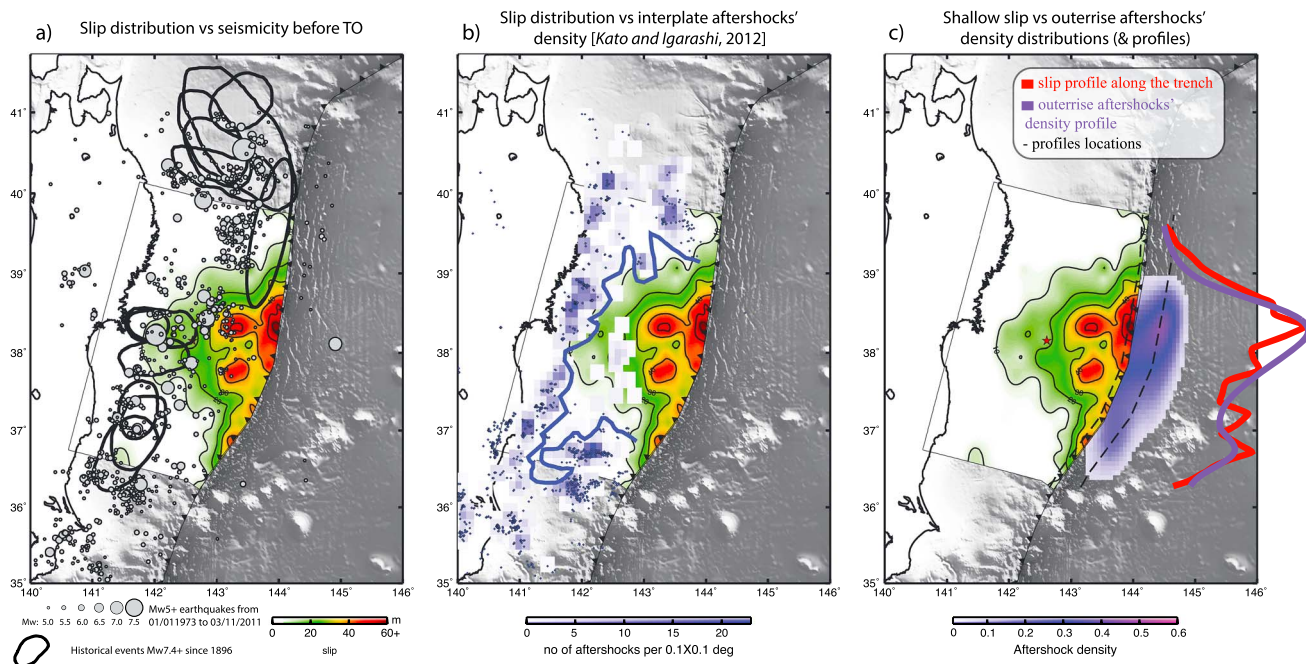


Figure 5. (a) TO slip distribution and historical seismicity prior to TO. Same as Figure 1 with black contours being $M_w 7.4+$ earthquakes since 1896 and gray circles, $M_w 5+$ earthquakes since 1973 (USGS catalog). Our slip distribution is located in a very low seismicity zone. (b) Our slip distribution compared to interplate aftershocks' density from *Kato and Igarashi* [2012]. Blue squares show aftershocks density during the 1 year period following TO, blue diamonds are repeating earthquakes, and the blue line is the coseismic rupture area delimited by *Kato and Igarashi* [2012]. Our slip distribution is in agreement with this limit. (c) Slip distribution at the free surface compared to outer-rise aftershocks' density (JMA catalog, 2 years following TO). We calculate two latitude profiles (dashed lines), one across our slip model at the trench (red) and one on the other side of the trench across the outer-rise aftershocks' density (purple). We see good correlations between the two profiles. It is coherent with the idea that large coseismic motion at the trench produces stress perturbations promoting normal faulting on the emergent subducting plate resulting in high outer-rise seismic activity.

stations of the Federation of Digital Seismograph Networks, well distributed in azimuth. The red curves show the corresponding synthetic RSTFs, computed from our spatiotemporal model, considering Love and Rayleigh waves phase velocities equal to 4.5 km/s and 3.8 km/s, respectively [Schwartz, 1999]. Because variations of the RSTFs as a function of station azimuth are directly related to the rupture process characteristics, the similarity between the observed and the computed RSTFs further validates our proposed source model.

6. Discussion

Detailed coseismic rupture imaging is a valuable resource to understand the physics of earthquakes. Thanks to the quantity of high-quality data—to our knowledge, it is the first time that so many data sets are inverted jointly—and especially the addition of tsunami records and improved modeling of their associated Green's functions, we obtain a robust and detailed slip model which can be compared to several independent observations to both challenge its validity and see if we can make progress in our understanding of the underlying physical processes.

6.1. Slip Distribution and Seismicity

In our present understanding of mega-earthquakes, coseismic patches are thought to correspond to locked portions of subduction interfaces loaded in stress [Kanda *et al.*, 2013]. These locked asperities should correspond to low-seismicity zones during long (possibly up to 1000 years) interseismic periods [Chlieh *et al.*, 2007; Perfettini *et al.*, 2010]. One purpose of joint inversions is to image this kind of asperities. Figure 5a shows the historical seismicity offshore northeast Japan/Honshu island since 1973 for moderate events, 1896 for large ones. We find that the large-slip zone is, as expected, located in a very low seismicity region. Indeed, we observe a clear deficit in both moderate ($M_w 6-M_w 7.5$) and large ($M_w > 7.5$) events in the 30m+ area of our preferred slip model. Most of the small events located in the red high-slip patch the closest to the epicenter are part of the foreshock sequence which started on 9 March 2011.

The seismicity rate of interplate earthquakes is expected to change significantly after the main shock, as a result of stress perturbations. Based on this hypothesis, *Kato and Igarashi* [2012] delineated the outer edge of the large-slip zone by calculating contrasts in interplate aftershocks density during the 1 year period following the main shock. We see in Figure 5b a good agreement between our slip distribution and their large-slip delineation, except in the southwest part of the fault plane. *Kato and Igarashi* [2012] suggest that this zone was affected by significant coseismic motion, although slip is not found in this particular area in most inversion slip models. Back projection studies [*Simons et al.*, 2011; *Ishii*, 2011; *Koper et al.*, 2011a, 2011b; *Meng et al.*, 2011; *Wang and Mori*, 2011; *Yao et al.*, 2011, 2012; *Zhang et al.*, 2011] suggest significant high-frequency seismic activity in this area. As we are interested in large-scale features of the slip distribution, we filter these high frequencies from our data. This makes our inversion insensitive to very small scale asperities. However, even though slip patterns of this amplitude (<10 m compared to the 60 m of main slip patches) are probably poorly resolved, we do obtain a slip patch in this region which reveals that some seismic moment is released (Figure 1).

After a subduction earthquake, seismicity is not only induced on the megathrust but in a much wider area. In particular, outer-rise aftershocks usually follow the main shock when the rupture propagates to the surface. Outer-rise earthquakes are defined as normal faulting earthquakes resulting from the extension of the oceanic plate as it enters the subduction zone, and a good measurement of this extension is the relative motion of the two plates at the trench, where the subduction starts. Consequently, after a large earthquake reaching the free surface, we expect an increase in the outer-rise aftershocks activity with an intensity proportional to the most surficial slip at the trench. We use JMA's catalog and calculate outer-rise aftershock density during the 2 years period following the main shock (for the density calculation, we used the SciPy algorithm of kernel-density estimate based on Gaussian kernels: http://docs.scipy.org/doc/scipy/reference/generated/scipy.stats.gaussian_kde.html). We calculate two latitude profiles (dashed lines in Figure 5c), one across our slip model at the trench (red) and one on the other side of the trench across the outer-rise aftershock density (purple). We notice a good correlation between the slip found at the trench and the density of aftershocks in the outer-rise region. This indicates that the shallowest part of our preferred slip model is spatially coherent with the seismicity independently observed in the incoming plate. Additionally, as this argument only applies to variations—and not absolute values—of slip along the trench, we are reminded that our model is in agreement with the 50 m of horizontal motion measured at the trench by *Fujiwara et al.* [2011].

As predicted by our current understanding of the different processes, our preferred slip model places most slip in a region where very low seismicity was recorded before TO, around which intense interplate aftershock activity is observed [*Sladen et al.*, 2010] and is also able to explain the induced seismic activity recorded in the incoming plate. These different results make our slip distribution model physically very consistent with the observed pre-TO and post-TO seismicity.

6.2. Stress Drop and Slab Interface Properties

In the last paragraph, we saw that our slip model agrees with independent observations of the seismicity in the region. To make a step further in the interpretation of this model, we now focus on a physical parameter that plays a critical role in the earthquake rupture process: the stress released on the fault during the rupture. We are not able to directly measure this stress drop, but we can derive its spatial distribution from our slip model.

The coseismic slip $\Delta u(x, y)$ on a fault area A in the x direction can be written as

$$\Delta u(x, y) = \frac{1}{4\pi^2} \int_{-\infty}^{+\infty} \int_{-\infty}^{+\infty} \Delta^* u(\xi, \eta) e^{-i(\xi x + \eta y)} d\xi d\eta \quad (1)$$

where

$$\Delta u^*(\xi, \eta) = \iint_A \Delta u(x, y) e^{i(\xi x + \eta y)} dx dy \quad (2)$$

The associated stress drop $\Delta\sigma$ is then given by

$$\Delta\sigma = \frac{\mu}{8\pi^2} \int_{-\infty}^{+\infty} \int_{-\infty}^{+\infty} \frac{2\gamma\xi^2 + \eta^2}{\sqrt{\xi^2 + \eta^2}} \Delta u^*(\xi, \eta) e^{-i(\xi x + \eta y)} d\xi d\eta \quad (3)$$

where λ and μ are Lamé constants and $\gamma = \frac{\lambda + \mu}{\lambda + 2\mu}$ [*Sato*, 1972; *Singh*, 1977].

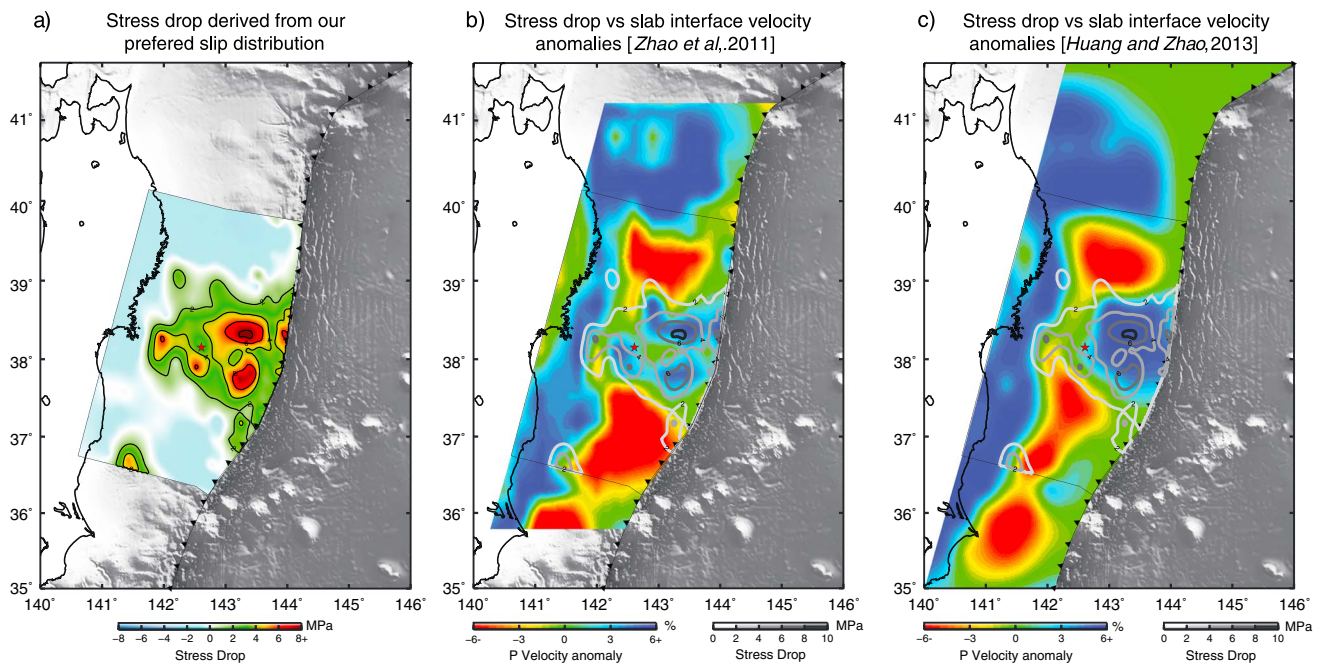


Figure 6. (a) Stress-drop distribution derived from our preferred slip model using the expression of Sato [1972] and Singh [1977]. Two large patches of stress drop exceeding 8 MPa are found at middistance between the epicenter and the trench. (b) Stress-drop distribution (gray to black contours) compared to the slab interface tomography of Zhao et al. [2011]. We see a very good correlation between blue high P wave velocity anomalies and large stress-drop patches. (c) Same as Figure 6b with the slab interface tomography of Huang and Zhao [2013].

We apply equation (3) to our preferred slip model and derive a stress-drop distribution along the fault (Figure 6). We find that the stress drop is dominated by two very large patches with amplitudes exceeding 8 MPa localized halfway between the epicenter and the trench. We observe two smaller patches (reaching 5 MPa) updip and near the hypocenter, another one in the south high-frequency zone discussed in section 6.1, and a last one close to the trench. The rest of the trench area is found to have released around 2 MPa such as the rest of the coseismic zone. The periphery of the coseismic zone is found to have experienced a slight stress increase (blue zone in Figure 6a).

Equation (3) does not include the effect of depth which implies that the free surface effect is neglected. This probably leads to an overestimation of the stress drop in the shallow part of the fault [Huang et al., 2014]. In this case, the deeper patches of very large stress drop are better candidates to explain most of the large energy radiation detected by seismic networks [Ishii, 2011], at least more than what is predicted by equation (3).

Large stress-drop patches like these are thought to be the consequence of the rupture of locked asperities loaded in stress during the interseismic period [Chlieh et al., 2007; Konca et al., 2008]. To release as much stress during an earthquake, it is straightforward to assume that these patches accumulated particularly large stress load before. These patches are then the most relevant information that our slip inversion provides about possible asperities distributed along the slab interface. Therefore, it is of particular interest to compare this stress-drop distribution with other sources of information on the slab interface properties.

The most common method for imaging such slab interface properties is inverting geodetic data to obtain the coupling rate (slip deficit at plate interface during the interseismic period compared to the tectonic convergence rate) along the fault. Many authors have tried to image the Japan slab coupling rate [Mazzotti et al., 2000; Hashimoto et al., 2009; Loveless and Meade, 2010, 2011; Perfettini and Avouac, 2014], but because of the narrow azimuthal coverage of the GPS network and its distance to the trench, the easternmost part of the slab (where large stress drop is found) lacks resolution even at large scale. Consequently, locked patches at the scale of interest cannot be imaged there. Following a very different approach, Zhao et al. [2011] and Huang and Zhao [2013] proposed tomography images of the slab interface. We compare the P wave velocity (V_p) anomalies variations along the slab revealed by their studies to our stress-drop

distribution (Figures 6b and 6c). We find a very good correlation between high V_p anomalies of Zhao *et al.*'s [2011] model and our stress-drop contours (Figure 6b). The two large stress-drop patches we imaged seem to match the few high-velocity anomalies in the eastern part of the fault. We also observe this correspondence for the smaller stress-drop patches. The 2 MPa isostress-drop line (which can be seen as the limit of the rupture) seems to follow the 0 velocity anomaly isoline. Huang and Zhao's [2013] model contains less details, but their larger-scale high-velocity anomaly east of the epicenter is also well correlated with our large stress-drop area (constituted by our two main patches). Zhao *et al.* [2011] and Huang and Zhao [2013] propose that the low-velocity anomalies might reflect the presence of sediments and fluids associated with slab dehydration and consequently to correspond to low coupled zones. On the other hand, they propose that high-velocity anomalies would be the signature of hard rock material constitutive of slab interface zones and are interpreted as highly coupled asperities. At least, consistent with this interpretation, low V_p (red zones) corresponds to low seismic activity while fast V_p (blues) corresponds to high occurrences of moderate to large earthquakes (Figures 5a and 6b or 6c). While the presence of sediments is not the only possible explanation for V_p anomalies, the correlation between our preferred slip model and the tomography results advocates for the idea that earthquake rupture and plate coupling are controlled by long-term features.

6.3. The Crucial Role of Normal Faulting in the Overriding Plate

In addition to these slab tomographies, we show, in Figure 7, another interesting particularity of the region: the presence of a large normal fault [Tsuji *et al.*, 2011, 2013] located just above our high-slip patch the closest to the epicenter and which coincides with our main stress-drop patch. There is no reported case of similar normal faults branching to the surface along the Japan subduction zone. Based on Cubas *et al.* [2013], the existence of this fault implies very low friction on the updip part of the megathrust of the region. This low friction authorizes large slip with low stress drop in this shallowest part of the region that we will define as block A, a coherent unit separated from block B by the normal fault (see illustration in Figure 7). We propose that the rupture of a long-term locked asperity on the megathrust (located below the normal fault) caused block A to move as a coherent unit with respect to block B, a motion made easier by a very low dynamic friction on the megathrust. The 1.1 m of offset measured at the surface of the normal fault and related to the coseismic phase [Tsuji *et al.*, 2013] (with possible larger amplitude at depth) attests for a partial block motion of this kind. This idea of block motion behavior is also consistent with the curious absence of aftershocks in the frontal wedge (defined here as block A) observed by Obana *et al.* [2013]. Indeed, if block A behaves as a coherent unit, internal deformation should be small.

Such a normal fault might be a mark of TO-type events. This idea was first proposed by Cubas *et al.* [2013] who brought the argument of the need of low friction on the megathrust to explain normal faulting on the overriding plate. The hypothesis of low friction would actually be confirmed around the same time from direct friction measurements on the shallowest part of the megathrust [Fulton *et al.*, 2013]. Until now, resolution in the published slip models did not permit to spatially link this normal fault to a high-slip patch at such a scale (Cubas *et al.* [2013] linked it to a slip pattern imaged by Wei *et al.* [2012] much larger than the supposed size of the normal fault). These high-slip patches—which appear to be coherent with independent observations (sections 6.1 and 6.2)—clearly point at the role of the normal fault in the rupture of TO, especially its link with extremely large shallow slip. As no other normal fault of this kind has been observed along the Honshu subduction zone outside the TO area, a consequence of this would be the relatively low likelihood for a TO-type event in another part of the subduction zone.

6.4. A Rupture Scenario to Reconcile the Different Observations

Based on the arguments above, we propose the following rupture scenario: the Tohoku-Oki earthquake started on 11 March 2011 at 14 h 56 (local time) as a magnitude $M_w 7$ like in a region where events of this size are common (see Figure 5a). After 40–50 s (see Figure 2), the rupture reached an asperity locked for a very long time—possibly since the 869 Jogan Sanriku earthquake [Minoura *et al.*, 2001; Sawai *et al.*, 2008]—inducing enough stress perturbation to cause its rupture. The rupture released an enormous amount of stress (main patch in Figure 6 associated with the STF peak in Figure 1) and lowered the effective friction of the part of the megathrust located updip—possibly by heating water contained in the thin scaly clay layer constituting the fault [Noda and Lapusta, 2013]—allowing block A to slip with negligible dynamic friction [Cubas *et al.*, 2013; Chester *et al.*, 2013; Ujiie *et al.*, 2013; Fulton *et al.*, 2013; Wang and Kinoshita, 2013]. The motion of block A, which is decoupled from block B by the large normal fault, allows it to slip freely with respect to both the incoming plate and the rest of the overriding plate. This could explain why the amount

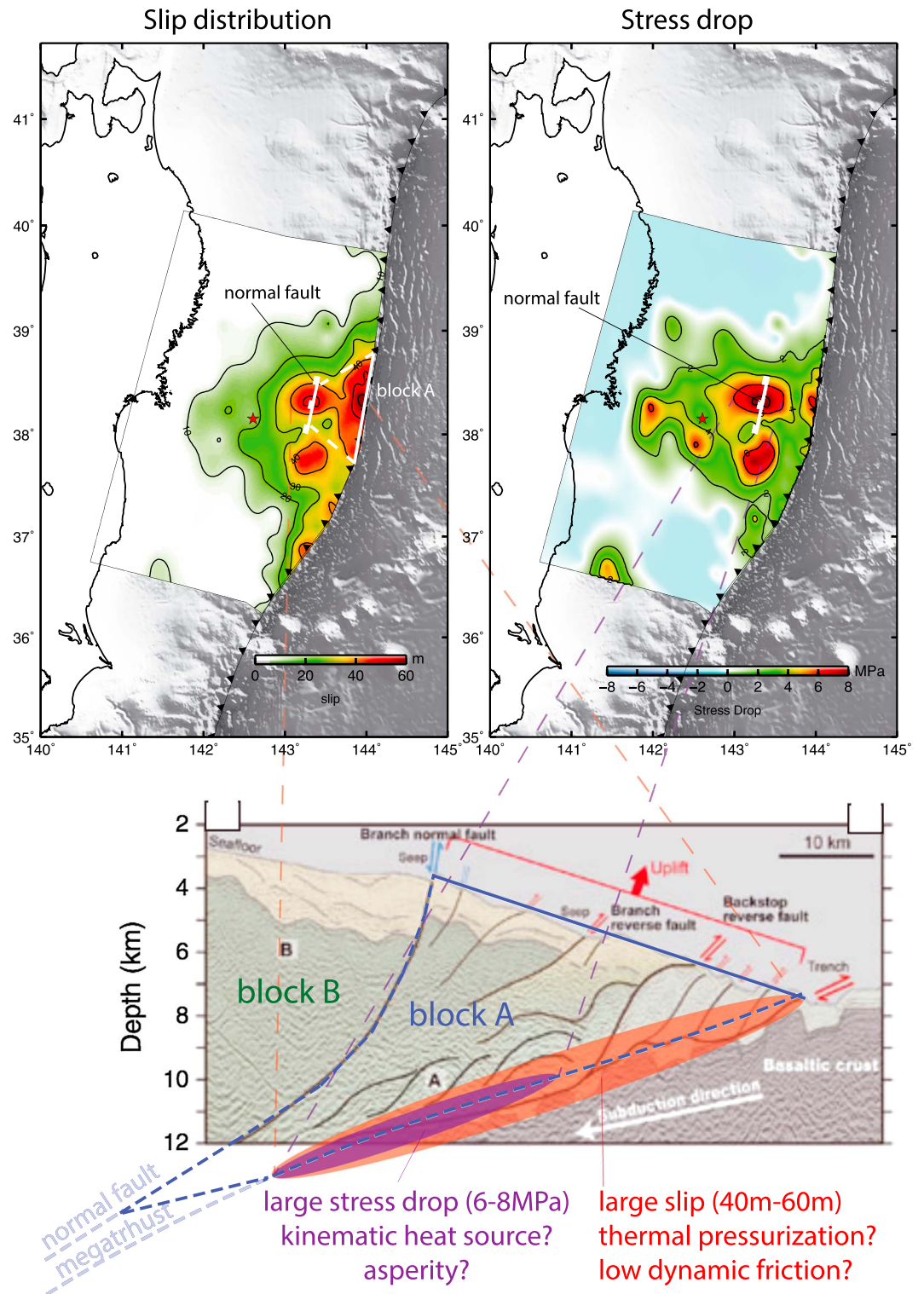


Figure 7. Illustrative sketch of the frontal wedge behavior in our proposed scenario. (top) Location of a large normal fault coseismically activated [Tsuji et al., 2011, 2013] in relation to slip (left) and stress-drop distributions (right). (bottom) Interpreted seismic profile (modified from Tsuji et al. [2011]) of the normal fault shown in top figures across the region affected by the largest slip. Blocks A (in blue) and B—separated by the large normal fault—moved by several meters in respect to each other [Tsuji et al., 2013].

of slip does not significantly decrease as the rupture reaches the free surface. The north and south borders of block A are not as clear as the normal and megathrust faults which can explain why the amount of slip slowly decreases from our higher-slip patch—located between the normal fault and the trench—to no slip on the north and south edges. In the south, the motion was accentuated by the rupture of a secondary asperity also associated with an important stress drop (second main path in Figure 6) causing more slip to reach the free surface south than north.

This scenario is close to the mechanism of tsunami earthquakes described by *Fukao* [1979] of a downdip earthquake nucleation inducing large shallow slip motion resulting in a large tsunami associated with a relatively low seismic moment; except here, the seismic moment is not small. And because the size of the Tohoku tsunami is coherent with the magnitude of the earthquake, it is not a tsunami earthquake as defined by *Kanamori* [1972]. This is also supported by the absence of a slow rupture component signature in far-field seismic records [*Okal*, 2013; *Han et al.*, 2013] (as well as by the relatively short source time function (Figures 1 and 2)), making the TO earthquake a very singular event among $M_w > 9.0$ mega-earthquakes: 1960 Valdivia ($M_w 9.5$), 1964 Alaska ($M_w 9.2$), and 2004 Sumatra ($M_w 9.1-9.3$) were all classified as tsunami earthquakes with a clear slow rupture component [*Okal*, 2013] and a deficit of seismic magnitude relatively to the induced tsunamis. For the most part, we explain the TO magnitude with the quasi-simultaneous ruptures of two localized asperities, a scenario also consistent with the focal mechanism simplicity observed by *Rivera and Kanamori* [2014].

Our interpretation, while still being a tentative scenario, allows to explain a number of observations: seismicity patterns before and after TO (Figure 5 [*Kato et al.*, 2012]), velocity anomalies imaged by tomography (Figure 6 [*Zhao et al.*, 2011; *Huang and Zhao*, 2013]), a normal fault revealed by geology (Figure 7 [*Tsuji et al.*, 2013]), rheological properties of the megathrust revealed by drilling [*Fulton et al.*, 2013; *Ujii et al.*, 2013; *Chester et al.*, 2013; *Wang and Kinoshita*, 2013], and even the absence of aftershocks in the frontal wedge [*Obana et al.*, 2013].

7. Conclusion

We performed a joint inversion including static GPS, strong motion, HRGPS, teleseismic, and tsunami records for the 11 March 2011 $M_w 9.0$ Tohoku-Oki earthquake to obtain a robust and detailed description of the rupture process (we choose to not include the seafloor geodesy measurements because of a probable large fraction of preseismic/postseismic signal). Our preferred slip model reveals a compact area of large slip, located updip of the epicenter and extending to the trench (see Figure 1). The large coseismic slip is found in an area previously characterized by very low seismicity (Figure 5a). The important interplate aftershock activity delineates the coseismic slip zone (see Figure 5b), while the density of outer-rise aftershocks is proportional to the amount of coseismic slip at the trench (see Figure 5c). All these observations make our slip model physically very coherent with patterns independently observed in the seismicity.

The stress-drop distribution, derived from our slip model, reveals two localized patches halfway between the hypocenter and the trench (see Figure 6). We find that these correlate with high V_p anomalies imaged by tomography of the slab interface, interpreted as highly coupled regions. We interpret these two patches as long-term-locked asperities explaining, for the most part, the exceptional magnitude of the event. Based on these results, we propose that the large shallow slip would be the consequence of an effective friction drop, due to thermal pressurization in the shallow part of the megathrust fault, initiated by the heat associated with the rupture of these two asperities.

The TO region presents a geological particularity: a large normal fault in the hanging wall, coseismically activated and not documented anywhere else along the Japan trench. *Cubas et al.* [2013] have shown that this normal fault can only be activated coseismically if the dynamic friction on the megathrust is very low, a condition which would also explain the large amount of slip reaching the free surface. If correct, this interpretation would indicate that TO-like earthquakes are unlikely elsewhere offshore North Japan. Our interpretation of the TO earthquake rupture is just a tentative scenario but deserves credit for explaining numerous independent measurements and being consistent about our knowledge of earthquake physics. Studies of the postseismic deformation of the frontal wedge will be of particular interest to challenge this proposed scenario.

Acknowledgments

In this paper we used static GPS data from the ARIA team at JPL/Caltech ([ftp://sideshow.jpl.nasa.gov/pub/usrsrc/ARIA/version0.3](http://sideshow.jpl.nasa.gov/pub/usrsrc/ARIA/version0.3)), 1 Hz GPS data from the GEONET network of the Geospatial Information Authority (GSI) of Japan, strong motion records from the Japanese network K-NET NIED data center (<http://www.kyoshin.bosai.go.jp>), teleseismic data from the Incorporated Research Institutions for Seismology (IRIS) data center, DART data from the NOAA National Geophysical Data Center (<http://ngdc.noaa.gov/hazard/dart/2011honshudart.html>), GPS buoys data given by the NOWPHAS system (<http://nowphas.mlit.go.jp/infoeng.html>), and CABLES data from the JAMSTEC cabled observatories website (<http://www.jamstec.go.jp/scdc/tope.html>). Earthquakes catalogs supporting Figures 5a and 5c were provided by the United States Geological Survey (USGS) (<http://earthquake.usgs.gov/regional/neic/>) and by the Japan Meteorological Agency (JMA) (on request). We used the SciPy algorithm of kernel-density estimate (http://docs.scipy.org/doc/scipy/reference/generated/scipy.stats.gaussian_kde.html) for the calculation of the aftershock density in Figure 5c. Data supporting Figures 5b, 6b, and 6c were kindly provided by A. Kato, D. Zhao, and Z. Huang. This work was partly supported by the ANR project TO-EOS, the French Ministry of Research and Education, the University of Nice Sophia-Antipolis (UNS), and the Centre National de la Recherche Scientifique (CNRS). We thank the UNS Centre de Calculs interactifs for computing time on its cluster (CICADA). We very much thank P. Bosser and F. Fund for their contribution in HRGPS data processing and Y. Yamazaki for providing his code (NEOWAVE) and for his valuable comments. We also thank K. Koketsu, H. Miyake, L. Rivera, N. Cubas, and Jean-Paul Ampuero for their valuable comments on this work.

References

- Ammon, C. J., T. Lay, H. Kanamori, and M. Cleveland (2011), A rupture model of the 2011 off the Pacific coast of Tohoku Earthquake, *Earth Planets Space*, *63*, 693–696, doi:10.5047/eps.2011.05.015.
- Bouchon, M. (1981), A simple method to calculate Green's functions for elastic layered media, *Bull. Seismol. Soc. Am.*, *71*(4), 959–971.
- Chester, F. M., et al. (2013), Structure and composition of the plate-boundary slip zone for the 2011 Tohoku-Oki earthquake, *Science*, *342*(6163), 1208–1211, doi:10.1126/science.1243719.
- Chlieh, M., et al. (2007), Coseismic slip and afterslip of the great Mw 9.15 Sumatra-Andaman earthquake of 2004, *Bull. Seismol. Soc. Am.*, *97*(1A), S152–S173, doi:10.1785/0120050631.
- Chu, R., S. Wei, D. V. Helmlinger, Z. Zhan, L. Zhu, and H. Kanamori (2011), Initiation of the great Mw 9.0 Tohoku-Oki earthquake, *Earth Planet. Sci. Lett.*, *308*(3–4), 277–283, doi:10.1016/j.epsl.2011.06.031.
- Cubas, N., J. Avouac, Y. Leroy, and A. Pons (2013), Low friction along the high slip patch of the 2011 Mw 9.0 Tohoku-Oki earthquake required from the wedge structure and extensional splay faults, *Geophys. Res. Lett.*, *40*, 4231–4237, doi:10.1002/grl.50682.
- Delouis, B., D. Giardini, P. Lundgren, and J. Salichon (2002), Joint inversion of InSAR, GPS, teleseismic, and strong-motion data for the spatial and temporal distribution of earthquake slip: Application to the 1999 zmit main shock, *Bull. Seismol. Soc. Am.*, *92*(1), 278–299, doi:10.1785/0120000806.
- Duputel, Z., P. S. Agram, M. Simons, S. E. Minson, and J. L. Beck (2014), Accounting for prediction uncertainty when inferring subsurface fault slip, *Geophys. J. Int.*, *197*(1), 464–482, doi:10.1093/gji/ggt517.
- Feng, G., and S. Jónsson (2012), Shortcomings of InSAR for studying megathrust earthquakes: The case of the Mw9.0 Tohoku-Oki earthquake, *Geophys. Res. Lett.*, *39*, L10305, doi:10.1029/2012GL051628.
- Fujii, Y., K. Satake, S. Sakai, M. Shinohara, and T. Kanazawa (2011), Tsunami source of the 2011 off the Pacific coast of Tohoku Earthquake, *Earth Planets Space*, *63*(7), 815–820, doi:10.5047/eps.2011.06.010.
- Fujiwara, T., S. Kodaira, T. No, Y. Kaiho, N. Takahashi, and Y. Kaneda (2011), The 2011 Tohoku-Oki earthquake: Displacement reaching the trench axis, *Science*, *334*(6060), 1240, doi:10.1126/science.1211554.
- Fukao, Y. (1979), Tsunami earthquakes and subduction processes near deep-sea trenches, *J. Geophys. Res.*, *84*(B5), 2303–2314, doi:10.1029/JB084iB05p02303.
- Fulton, P. M., et al. (2013), Low coseismic friction on the Tohoku-Oki fault determined from temperature measurements, *Science*, *342*(6163), 1214–1217, doi:10.1126/science.1243641.
- Han, S.-C., R. Riva, J. Sauber, and E. Okal (2013), Source parameter inversion for recent great earthquakes from a decade-long observation of global gravity fields, *J. Geophys. Res. Solid Earth*, *118*, 1240–1267, doi:10.1002/jgrb.50116.
- Hartzell, S. H. (1978), Earthquake aftershocks as Green's functions, *Geophys. Res. Lett.*, *5*(1), 1–4, doi:10.1029/GL005i001p00001.
- Hashimoto, C., A. Noda, T. Sagiya, and M. Matsuura (2009), Interplate seismogenic zones along the Kuril Japan trench inferred from GPS data inversion, *Nat. Geosci.*, *2*(2), 141–144, doi:10.1038/ngeo421.
- Hayes, G. P. (2011), Rapid source characterization of the 2011 Mw 9.0 off the Pacific coast of Tohoku earthquake, *Earth Planets Space*, *63*(7), 529–534, doi:10.5047/eps.2011.05.012.
- Hayes, G. P., D. J. Wald, and R. L. Johnson (2012), Slab1.0: A three-dimensional model of global subduction zone geometries, *J. Geophys. Res.*, *117*, B01302, doi:10.1029/2011JB008524.
- Hooper, A., et al. (2013), Importance of horizontal seafloor motion on tsunami height for the 2011 Mw = 9.0 Tohoku-Oki earthquake, *Earth Planet. Sci. Lett.*, *361*, 469–479, doi:10.1016/j.epsl.2012.11.013.
- Huang, Y., J.-P. Ampuero, and H. Kanamori (2014), Slip-weakening models of the 2011 Tohoku-Oki earthquake and constraints on stress drop and fracture energy, *Pure Appl. Geophys.*, *1*–14, doi:10.1007/s00024-013-0718-2.
- Huang, Z., and D. Zhao (2013), Mechanism of the 2011 Tohoku-Oki earthquake (Mw 9.0) and tsunami: Insight from seismic tomography, *J. Asian Earth Sci.*, *70*–71, 160–168, doi:10.1016/j.jseaes.2013.03.010.
- Ide, S., A. Baltay, and G. C. Beroza (2011), Shallow dynamic overshoot and energetic deep rupture in the 2011 Mw 9.0 Tohoku-Oki earthquake, *Science*, *332*(6036), 1426–1429, doi:10.1126/science.1207020.
- Iinuma, T., M. Ohzono, Y. Ohta, and S. Miura (2011), Coseismic slip distribution of the 2011 off the Pacific coast of Tohoku Earthquake (M 9.0) estimated based on GPS data—Was the asperity in Miyagi-Oki ruptured?, *Earth Planets Space*, *63*(7), 643–648, doi:10.5047/eps.2011.06.013.
- Iinuma, T., et al. (2012), Coseismic slip distribution of the 2011 off the Pacific coast of Tohoku Earthquake (M9.0) refined by means of seafloor geodetic data, *J. Geophys. Res.*, *117*, B07409, doi:10.1029/2012JB009186.
- Ishii, M. (2011), High-frequency rupture properties of the Mw 9.0 off the Pacific coast of Tohoku earthquake, *Earth Planets Space*, *63*(7), 609–614, doi:10.5047/eps.2011.07.009.
- Ito, T., K. Ozawa, T. Watanabe, and T. Sagiya (2011), Slip distribution of the 2011 off the Pacific coast of Tohoku Earthquake inferred from geodetic data, *Earth Planets Space*, *63*(7), 627–630, doi:10.5047/eps.2011.06.023.
- Kajiura, K. (1963), The leading wave of a tsunami, *Bull. Earthquake Res. Inst.*, *41*(33), 535–571.
- Kanamori, H. (1972), Mechanism of tsunami earthquakes, *Phys. Earth Planet. Inter.*, *6*(5), 346–359, doi:10.1016/0031-9201(72)90058-1.
- Kanda, R. V. S., E. A. Hetland, and M. Simons (2013), An asperity model for fault creep and interseismic deformation in northeastern Japan, *Geophys. J. Int.*, *192*(1), 38–57, doi:10.1093/gji/ggs028.
- Kato, A., and T. Igarashi (2012), Regional extent of the large coseismic slip zone of the 2011 Mw 9.0 Tohoku-Oki earthquake delineated by on-fault aftershocks, *Geophys. Res. Lett.*, *39*, L15301, doi:10.1029/2012GL052220.
- Kato, A., K. Obara, T. Igarashi, H. Tsuruoka, S. Nakagawa, and N. Hirata (2012), Propagation of slow slip leading up to the 2011 Mw 9.0 Tohoku-Oki earthquake, *Science*, *335*(6069), 705–708, doi:10.1126/science.1215141.
- Kido, M., Y. Osada, H. Fujimoto, R. Hino, and Y. Ito (2011), Trench-normal variation in observed seafloor displacements associated with the 2011 Tohoku-Oki earthquake, *Geophys. Res. Lett.*, *38*, L24303, doi:10.1029/2011GL050057.
- Koketsu, K., et al. (2011), A unified source model for the 2011 Tohoku earthquake, *Earth Planet. Sci. Lett.*, *310*(3–4), 480–487, doi:10.1016/j.epsl.2011.09.009.
- Konca, A. O., et al. (2008), Partial rupture of a locked patch of the Sumatra megathrust during the 2007 earthquake sequence, *Nature*, *456*(7222), 631–635, doi:10.1038/nature07572.
- Koper, K. D., A. R. Hutko, and T. Lay (2011a), Along-dip variation of teleseismic short-period radiation from the 11 March 2011 Tohoku earthquake (Mw 9.0), *Geophys. Res. Lett.*, *38*, L21309, doi:10.1029/2011GL049689.
- Koper, K. D., A. R. Hutko, T. Lay, C. J. Ammon, and H. Kanamori (2011b), Frequency-dependent rupture process of the 2011 Mw 9.0 Tohoku earthquake: Comparison of short-period p wave back projection images and broadband seismic rupture models, *Earth Planets Space*, *63*(7), 599–602, doi:10.5047/eps.2011.05.026.

- Lay, T., Y. Yamazaki, C. J. Ammon, K. F. Cheung, and H. Kanamori (2011a), The 2011 Mw 9.0 off the Pacific coast of Tohoku earthquake: Comparison of deep-water tsunami signals with finite-fault rupture model predictions, *Earth Planets Space*, *63*(7), 797–801, doi:10.5047/eps.2011.05.03.
- Lay, T., C. J. Ammon, H. Kanamori, L. Xue, and M. J. Kim (2011b), Possible large near-trench slip during the 2011 Mw 9.0 off the Pacific coast of Tohoku earthquake, *Earth Planets Space*, *63*(7), 687–692, doi:10.5047/eps.2011.05.033.
- Lee, S.-J., B.-S. Huang, M. Ando, H.-C. Chiu, and J.-H. Wang (2011), Evidence of large scale repeating slip during the 2011 Tohoku-Oki earthquake, *Geophys. Res. Lett.*, *38*, L19306, doi:10.1029/2011GL049580.
- Loveless, J. P., and B. J. Meade (2010), Geodetic imaging of plate motions, slip rates, and partitioning of deformation in Japan, *J. Geophys. Res.*, *115*, B02410, doi:10.1029/2008JB006248.
- Loveless, J. P., and B. J. Meade (2011), Spatial correlation of interseismic coupling and coseismic rupture extent of the 2011 MW = 9.0 Tohoku-Oki earthquake, *Geophys. Res. Lett.*, *38*, L17306, doi:10.1029/2011GL048561.
- Maeda, T., T. Furumura, S. Sakai, and M. Shinohara (2011), Significant tsunami observed at ocean-bottom pressure gauges during the 2011 off the Pacific coast of Tohoku earthquake, *Earth Planets Space*, *63*(7), 803–808, doi:10.5047/eps.2011.06.005.
- Mazzotti, S., X. Le Pichon, P. Henry, and S.-I. Miyazaki (2000), Full interseismic locking of the Nankai and Japan-west Kurile subduction zones: An analysis of uniform elastic strain accumulation in Japan constrained by permanent GPS, *J. Geophys. Res.*, *105*(B6), 13,159–13,177, doi:10.1029/2000JB900060.
- Melgar, D., and Y. Bock (2013), Near-field tsunami models with rapid earthquake source inversions from land- and ocean-based observations: The potential for forecast and warning, *J. Geophys. Res. Solid Earth*, *118*, 5939–5955, doi:10.1002/2013JB010506.
- Meng, L., A. Inbal, and J.-P. Ampuero (2011), A window into the complexity of the dynamic rupture of the 2011 Mw 9 Tohoku-Oki earthquake, *Geophys. Res. Lett.*, *38*, L00G07, doi:10.1029/2011GL048118.
- Minoura, K., F. Imamura, D. Sugawara, Y. Kono, and T. Iwashita (2001), The 869 Jogan tsunami deposit and recurrence interval of large-scale tsunami on the Pacific coast of northeast Japan, *J. Nat. Disaster Sci.*, *23*(2), 83–88.
- Minson, S. E., M. Simons, J. L. Beck, F. Ortega, J. Jiang, S. E. Owen, A. W. Moore, A. Inbal, and A. Sladen (2014), Bayesian inversion for finite fault earthquake source models—II: The 2011 great Tohoku-Oki, Japan earthquake, *Geophys. J. Int.*, *198*(2), 922–944.
- Miyazaki, S., J. J. McGuire, and P. Segall (2011), Seismic and aseismic fault slip before and during the 2011 off the Pacific coast of Tohoku earthquake, *Earth Planets and Space*, *63*(7), 637–642, doi:10.5047/eps.2011.07.001.
- Nabelek, J. L. (1984), Determination of earthquake source parameters from inversion of body waves, PhD thesis, M. I. T., Dept. of Earth, Atmospheric and Planetary Sciences, Cambridge, Mass.
- Nettles, M., G. Ekstrom, and H. C. Koss (2011), Centroid-moment-tensor analysis of the 2011 off the Pacific coast of Tohoku earthquake and its larger foreshocks and aftershocks, *Earth Planets Space*, *63*(7), 519–523.
- Noda, H., and N. Lapusta (2013), Stable creeping fault segments can become destructive as a result of dynamic weakening, *Nature*, *493*(7433), 518–521, doi:10.1038/nature11703.
- Obana, K., et al. (2013), Aftershocks near the updip end of the 2011 Tohoku-Oki earthquake, *Earth Planet. Sci. Lett.*, *382*, 111–116, doi:10.1016/j.epsl.2013.09.007.
- Okal, E. A. (2013), From 3-hz p waves to 0 s 2: No evidence of a slow component to the source of the 2011 Tohoku earthquake, *Pure Appl. Geophys.*, *170*(6–8), 963–973, doi:10.1007/s00024-012-0500-x.
- Ozawa, S., T. Nishimura, H. Suito, T. Kobayashi, M. Tobita, and T. Imakiire (2011), Coseismic and postseismic slip of the 2011 magnitude-9 Tohoku-Oki earthquake, *Nature*, *475*(7356), 373–376, doi:10.1038/nature10227.
- Perfettini, H., and J. P. Avouac (2014), The seismic cycle in the area of the 2011 Mw9.0 Tohoku-Oki earthquake, *J. Geophys. Res. Solid Earth*, *119*, 4469–4515, doi:10.1002/2013JB010697.
- Perfettini, H., et al. (2010), Seismic and aseismic slip on the Central Peru megathrust, *Nature*, *465*(7294), 78–81, doi:10.1038/nature09062.
- Rivera, L., and H. Kanamori (2014), Diagnosing source geometrical complexity of large earthquakes, *Pure and Applied Geophysics*, 1–22, doi:10.1007/s00024-013-0769-4.
- Romano, F., A. Piatanesi, S. Lorito, N. D'Agostino, K. Hirata, S. Atzori, Y. Yamazaki, and M. Cocco (2012), Clues from joint inversion of tsunami and geodetic data of the 2011 Tohoku-Oki earthquake, *Sci. Rep.*, *2*, 385, doi:10.1038/srep00385.
- Saito, T., Y. Ito, D. Inazu, and R. Hino (2011), Tsunami source of the 2011 Tohoku-Oki earthquake, Japan: Inversion analysis based on dispersive tsunami simulations, *Geophys. Res. Lett.*, *38*, L00G19, doi:10.1029/2011GL049089.
- Satake, K., Y. Fujii, T. Harada, and Y. Namegaya (2013), Time and space distribution of coseismic slip of the 2011 Tohoku earthquake as inferred from tsunami waveform data, *Bull. Seismol. Soc. Am.*, *103*(2B), 1473–1492, doi:10.1785/0120120122.
- Sato, M., T. Ishikawa, N. Ujihara, S. Yoshida, M. Fujita, M. Mochizuki, and A. Asada (2011), Displacement above the hypocenter of the 2011 Tohoku-Oki earthquake, *Science*, *332*(6036), 1395–1395, doi:10.1126/science.1207401.
- Sato, R. (1972), Stress drop for a finite fault, *J. Phys. Earth*, *20*(4), 397–407.
- Savage, J. C. (1980), Dislocations in seismology, in *Dislocations in Solids*, edited by F. R. N. Nabarro, pp. 251–339, North-Holland, New York.
- Sawai, Y., Y. Fujii, O. Fujiwara, T. Kamataki, J. Komatsubara, Y. Okamura, K. Satake, and M. Shishikura (2008), Marine incursions of the past 1500 years and evidence of tsunamis at Suijin-numa, a coastal lake facing the Japan Trench, *The Holocene*, *18*(4), 517–528.
- Schwartz, S. Y. (1999), Noncharacteristic behavior and complex recurrence of large subduction zone earthquakes, *J. Geophys. Res.*, *104*(B10), 23,111–23,125, doi:10.1029/1999JB900226.
- Shao, G., X. Li, C. Ji, and T. Maeda (2011), Focal mechanism and slip history of the 2011 Mw 9.1 off the Pacific coast of Tohoku earthquake, constrained with teleseismic body and surface waves, *Earth Planets Space*, *63*(7), 559–564, doi:10.5047/eps.2011.06.028.
- Simons, M., et al. (2011), The 2011 magnitude 9.0 Tohoku-Oki earthquake: Mosaicking the megathrust from seconds to centuries, *Science*, *332*(6036), 1421–1425, doi:10.1126/science.1206731.
- Singh, S. K. (1977), Slip and stress drop on a circular fault, *Bull. Seismol. Soc. Am.*, *67*(2), 279–284.
- Sladen, A., H. Tavera, M. Simons, J. P. Avouac, A. O. Konca, H. Perfettini, L. Audin, E. J. Fielding, F. Ortega, and R. Cavagnoud (2010), Source model of the 2007 Mw 8.0 Pisco, Peru earthquake: Implications for seismogenic behavior of subduction megathrusts, *J. Geophys. Res.*, *115*, B02405, doi:10.1029/2009JB006429.
- Takahashi, N., et al. (2004), Seismic structure and seismogenesis off Sanriku region, northeastern Japan, *Geophys. J. Int.*, *159*(1), 129–145, doi:10.1111/j.1365-246X.2004.02350.x.
- Tanioka, Y., and K. Satake (1996), Tsunami generation by horizontal displacement of ocean bottom, *Geophys. Res. Lett.*, *23*(8), 861–864, doi:10.1029/96GL00736.
- Tsai, V. C., J.-P. Ampuero, H. Kanamori, and D. J. Stevenson (2013), Estimating the effect of Earth elasticity and variable water density on tsunami speeds, *Geophys. Res. Lett.*, *40*, 492–496, doi:10.1002/grl.50147.
- Tsuji, T., Y. Ito, M. Kido, Y. Osada, H. Fujimoto, J. Ashi, M. Kinoshita, and T. Matsuoka (2011), Potential tsunamigenic faults of the 2011 off the Pacific coast of Tohoku Earthquake, *Earth Planets Space*, *63*(7), 831–834, doi:10.5047/eps.2011.05.028.

- Tsuji, T., K. Kawamura, T. Kanamatsu, T. Kasaya, K. Fujikura, Y. Ito, T. Tsuru, and M. Kinoshita (2013), Extension of continental crust by anelastic deformation during the 2011 Tohoku-Oki earthquake: The role of extensional faulting in the generation of a great tsunami, *Earth Planet. Sci. Lett.*, *364*, 44–58, doi:10.1016/j.epsl.2012.12.038.
- Ujii, K., et al. (2013), Low coseismic shear stress on the Tohoku-Oki megathrust determined from laboratory experiments, *Science*, *342*(6163), 1211–1214, doi:10.1126/science.1243485.
- Vallée, M. (2004), Stabilizing the empirical Green function analysis: Development of the projected Landweber method, *Bull. Seismol. Soc. Am.*, *94*(2), 394–409.
- Wang, D., and J. Mori (2011), Rupture process of the 2011 off the Pacific coast of Tohoku earthquake (M_w 9.0) as imaged with back-projection of teleseismic P-waves, *Earth Planets Space*, *63*(7), 603–607, doi:10.5047/eps.2011.05.029.
- Wang, K., and M. Kinoshita (2013), Dangers of being thin and weak, *Science*, *342*(6163), 1178–1180, doi:10.1126/science.1246518.
- Watada, S. (2013), Tsunami speed variations in density-stratified compressible global oceans, *Geophys. Res. Lett.*, *40*, 4001–4006, doi:10.1002/grl.50785.
- Wei, S., R. Graves, D. Helmberger, J.-P. Avouac, and J. Jiang (2012), Sources of shaking and flooding during the Tohoku-Oki earthquake: A mixture of rupture styles, *Earth Planet. Sci. Lett.*, *333*, 91–100, doi:10.1016/j.epsl.2012.04.006.
- Yamazaki, Y., Z. Kowalik, and K. Fai Cheung (2009), Depth-integrated, non-hydrostatic model for wave breaking and run-up, *Int. J. Numer. Methods Fluids*, *61*(5), 473–497.
- Yamazaki, Y., T. Lay, K. F. Cheung, H. Yue, and H. Kanamori (2011a), Modeling near-field tsunami observations to improve finite-fault slip models for the 11 March 2011 Tohoku earthquake, *Geophys. Res. Lett.*, *38*, L00G15, doi:10.1029/2011GL049130.
- Yamazaki, Y., K. F. Cheung, and Z. Kowalik (2011b), Depth-integrated, non-hydrostatic model with grid nesting for tsunami generation, propagation, and run-up, *Int. J. Numer. Methods Fluids*, *67*, 2081–2107.
- Yamazaki, Y., K. F. Cheung, and T. Lay (2013), Modeling of the 2011 Tohoku near-field tsunami from finite-fault inversion of seismic waves, *Bull. Seismol. Soc. Am.*, *103*(2B), 1444–1455, doi:10.1785/0120120103.
- Yao, H., P. Gerstoft, P. M. Shearer, and C. Mecklenbräuker (2011), Compressive sensing of the Tohoku-Oki Mw 9.0 earthquake: Frequency-dependent rupture modes, *Geophys. Res. Lett.*, *38*, L20310, doi:10.1029/2011GL049223.
- Yao, H., P. M. Shearer, and P. Gerstoft (2012), Subevent location and rupture imaging using iterative backprojection for the 2011 Tohoku Mw 9.0 earthquake, *Geophys. J. Int.*, *190*(2), 1152–1168, doi:10.1111/j.1365-246X.2012.05541.x.
- Yokota, Y., K. Koketsu, Y. Fujii, K. Satake, S. Sakai, M. Shinohara, and T. Kanazawa (2011), Joint inversion of strong motion, teleseismic, geodetic, and tsunami datasets for the rupture process of the 2011 Tohoku earthquake, *Geophys. Res. Lett.*, *38*, L00G21, doi:10.1029/2011GL050098.
- Yoshida, K., A. Hasegawa, T. Okada, T. Iinuma, Y. Ito, and Y. Asano (2012), Stress before and after the 2011 great Tohoku-Oki earthquake and induced earthquakes in inland areas of eastern Japan, *Geophys. Res. Lett.*, *39*, L03302, doi:10.1029/2011GL049729.
- Yoshida, Y., H. Ueno, D. Muto, and S. Aoki (2011), Source process of the 2011 off the Pacific coast of Tohoku earthquake with the combination of teleseismic and strong motion data, *Earth Planets Space*, *63*(7), 565–569.
- Yue, H., and T. Lay (2013), Source rupture models for the Mw 9.0 2011 Tohoku earthquake from joint inversions of highrate geodetic and seismic data, *Bull. Seismol. Soc. Am.*, *103*(2B), 1242–1255, doi:10.1785/0120120119.
- Zhang, H., Z. Ge, and L. Ding (2011), Three sub-events composing the 2011 off the Pacific coast of Tohoku earthquake (M_w 9.0) inferred from rupture imaging by back-projecting teleseismic P waves, *Earth Planets Space*, *63*(7), 595–598, doi:10.5047/eps.2011.06.021.
- Zhao, D., Z. Huang, N. Umino, A. Hasegawa, and H. Kanamori (2011), Structural heterogeneity in the megathrust zone and mechanism of the 2011 Tohoku-Oki earthquake (M_w 9.0), *Geophys. Res. Lett.*, *38*, L17308, doi:10.1029/2011GL048408.